Supporting Information Available

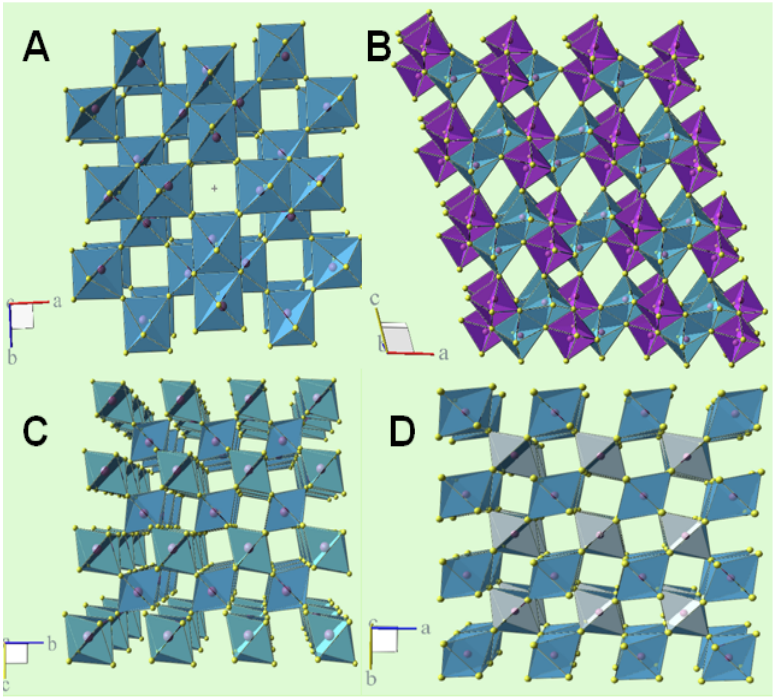

Figure S1. Schematic depictions of the crystal structure of commonly synthesized VO_2 polymorphs. **(A)** metastable tetragonal VO_2 (A) **(B)** metastable monoclinic VO_2 (B) **(C)** monoclinic M1, and (**D**) tetragonal rutile VO_2.

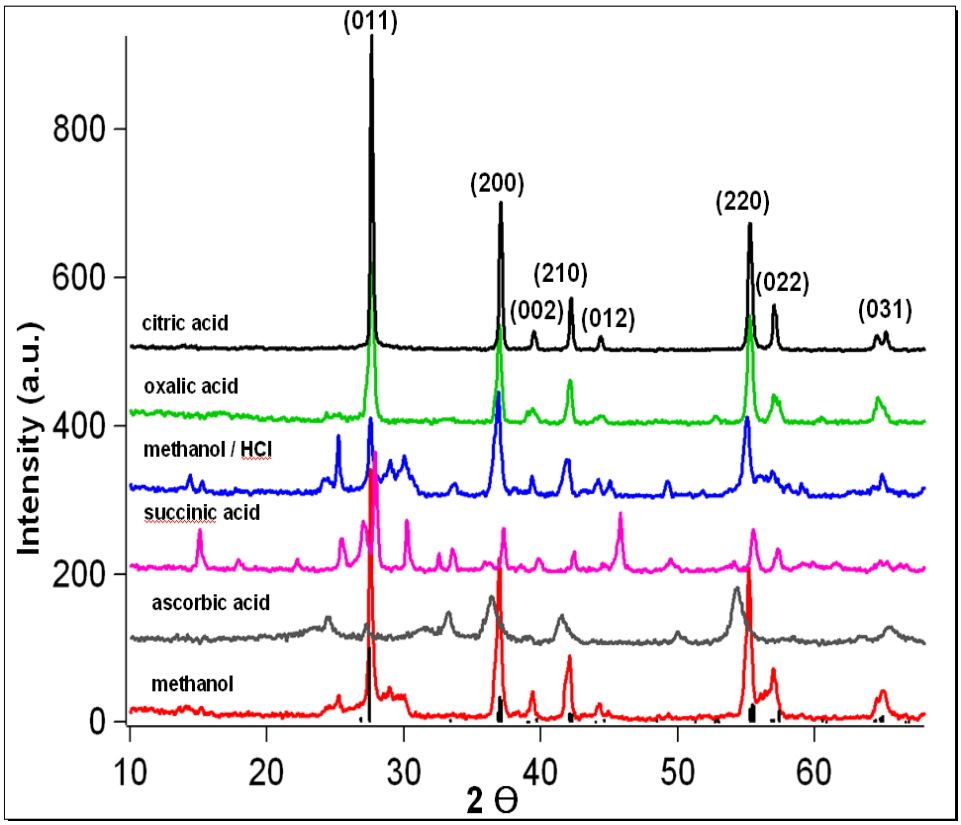

Figure S2. XRD patterns of VO_2 nanostructures prepared by the hydrothermal reduction of bulk V_2O_5 using different structure-directing templates and mild reducing agents

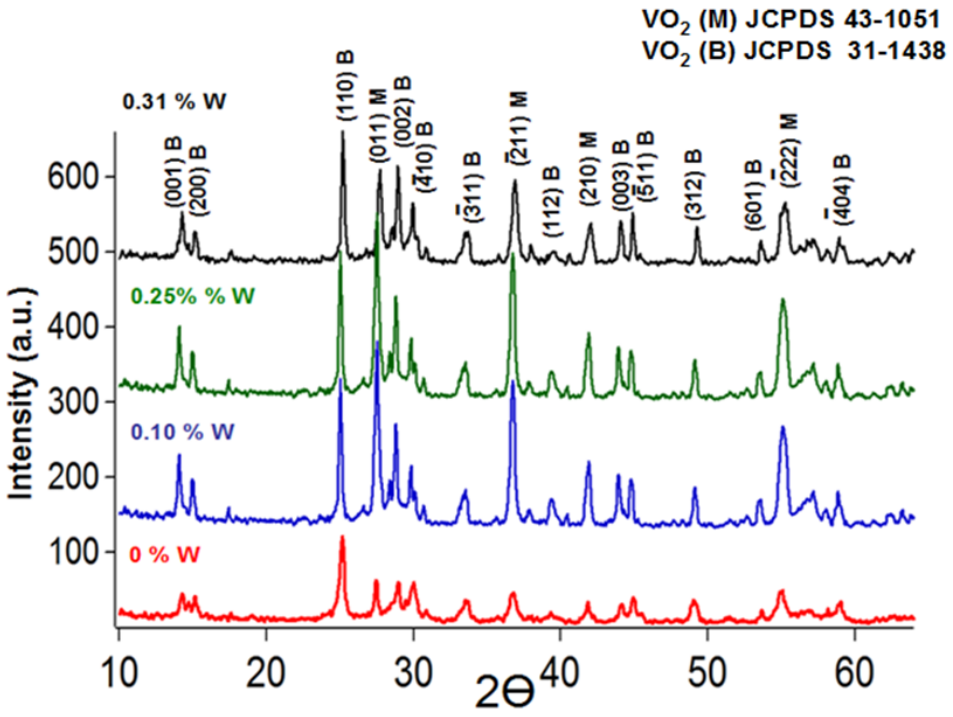

Figure S3. Powder X-ray diffraction patterns of $W_xV_{1-x}O_2$ nanostructures obtained at tungsten dopant concentrations <0.40 at. % indicating the substantial contributions from VO_2(B) phases.

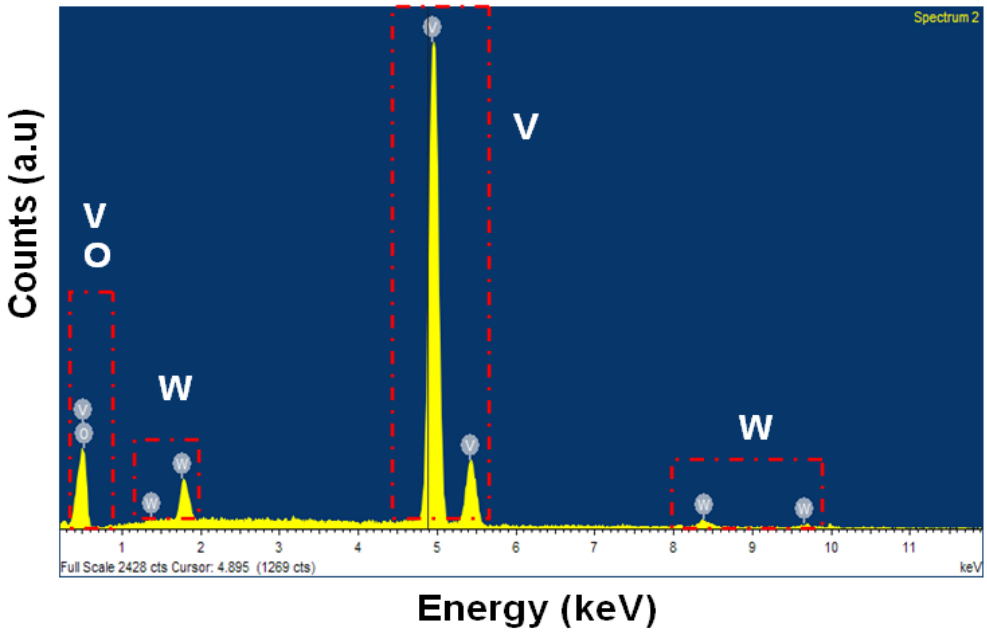

Figure S4. Energy-dispersive X-ray spectra showing the presence of W, V, and O elements in the as-synthesized W-doped VO_2 nanostructures.

Morphology variations as a function of reaction variables

Figure S5 (Supporting Information) shows the morphologies of $W_xV_{1-x}O_2$ nanostructures prepared by the hydrothermal reduction of V_2O_5 using methanol, oxalic acid, citric acid, and ascorbic acid for 72 h. The first three yield monodisperse well-defined 1D nanostructures, whereas reduction with ascorbic acid yields poorly structured nanoparticulates. Figure S6 (Supporting Information) shows the influence of the reaction temperature on the morphologies of the nanostructure for the oxalic acid reduction of V_2O_5 for 72 h. It is clearly evident that the products formed after reaction at 180 and 210°C are polydisperse nanoparticulates and short nanobelts, consistent with the predominance of the metastable VO_2(B) phase under these conditions. Figure S7 (Supporting Information) shows the influence of the reaction time for the oxalic acid reduction of V_2O_5 in the presence of 20 mg of H_2WO_4. Again, consistent with the XRD patterns in Figure 2, well-defined 1D nanostructures are observed only after 48 h of reaction as the structures recrystallize into the rutile/monoclinic polymorphs, whereas remnant metastable VO_2(B) synthesized at lower temperatures adopts morphologies with relatively poorly defined geometries.

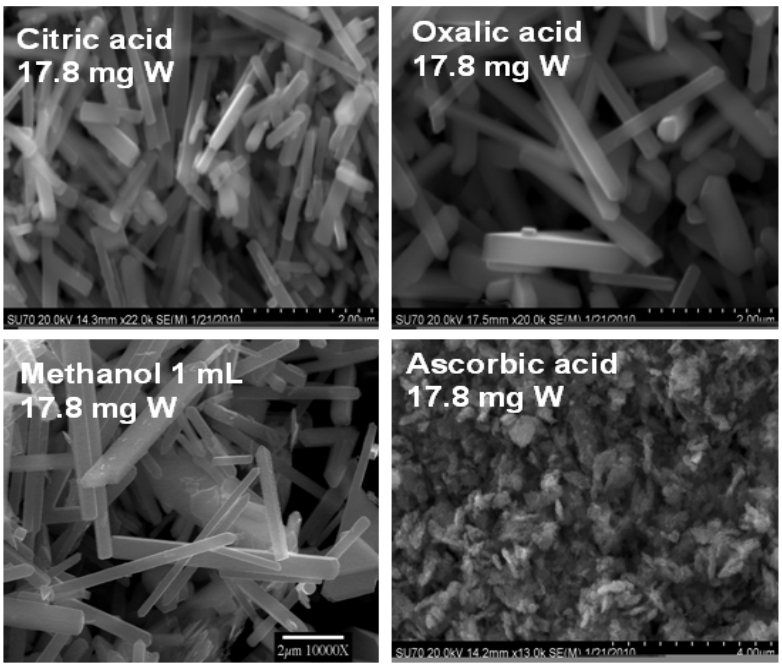

Figure S5. SEM images for as-prepared $W_xV_{1-x}O_2$ nanostructures under different reducing agents

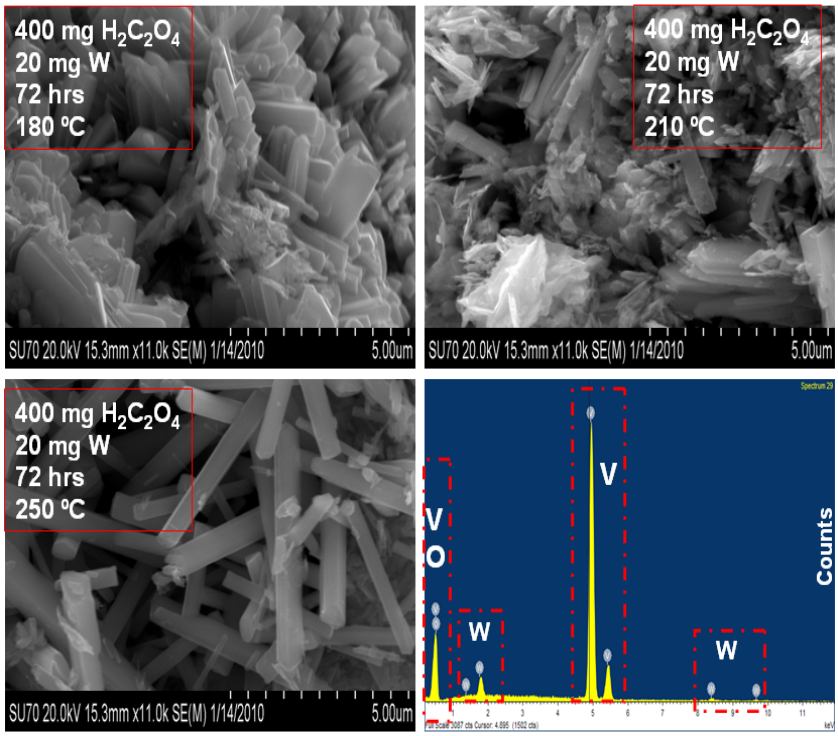

Figure S6. SEM images for as-prepared $W_xV_{1-x}O_2$ nanostructures under different reaction temperatures. The EDX spectrum corroborates the presence of W, V, and O within the nanostructures.

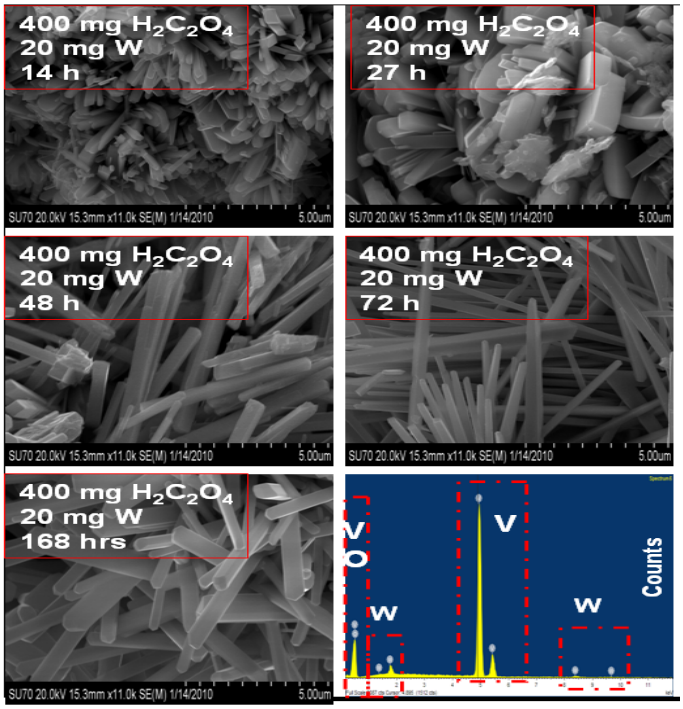

Figure S7. SEM images for as-prepared $W_xV_{1-x}O_2$ nanostructures prepared at different reaction times. The EDX spectrum further corroborates W doping within the nanostructures.

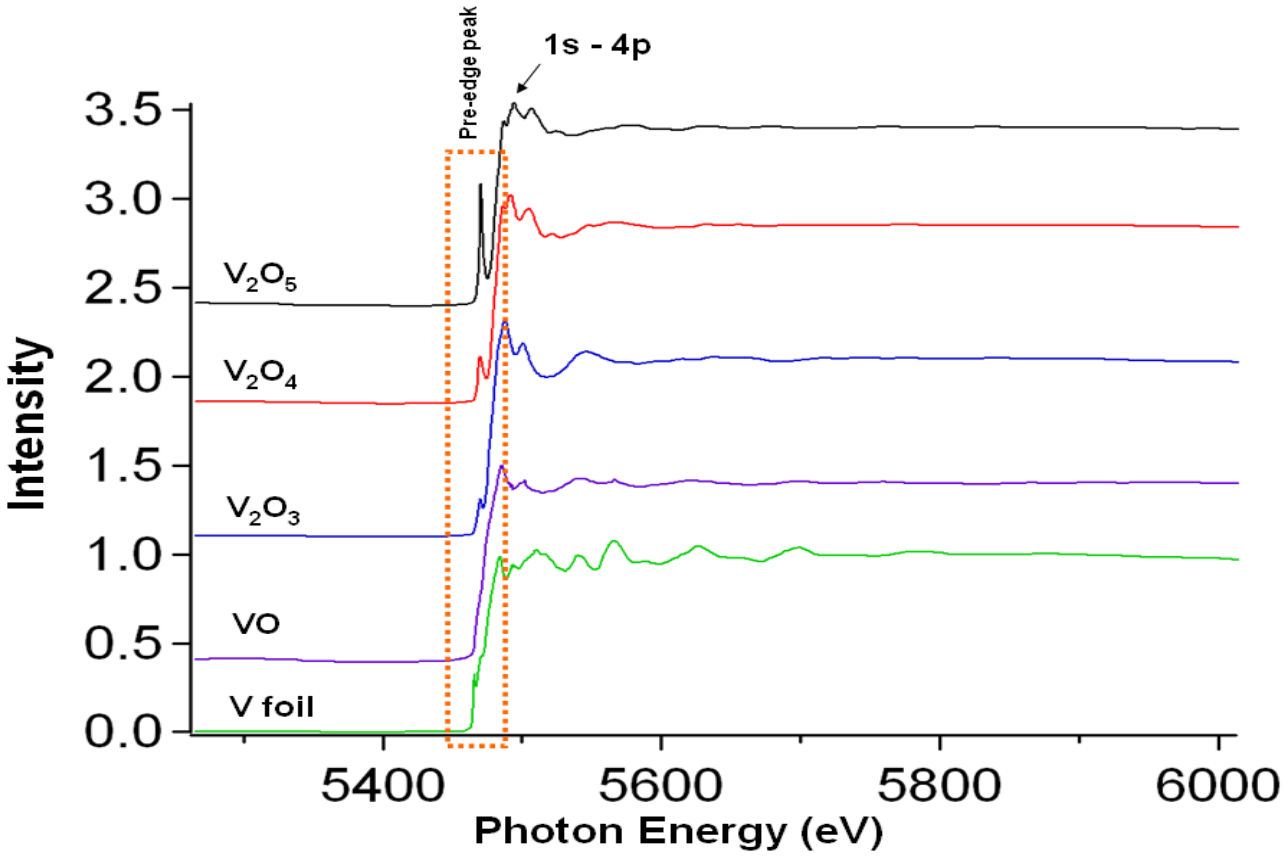

Figure S8. V K-edge XAFS spectra obtained at room temperature for several binary vanadium oxide and vanadium foil standards.

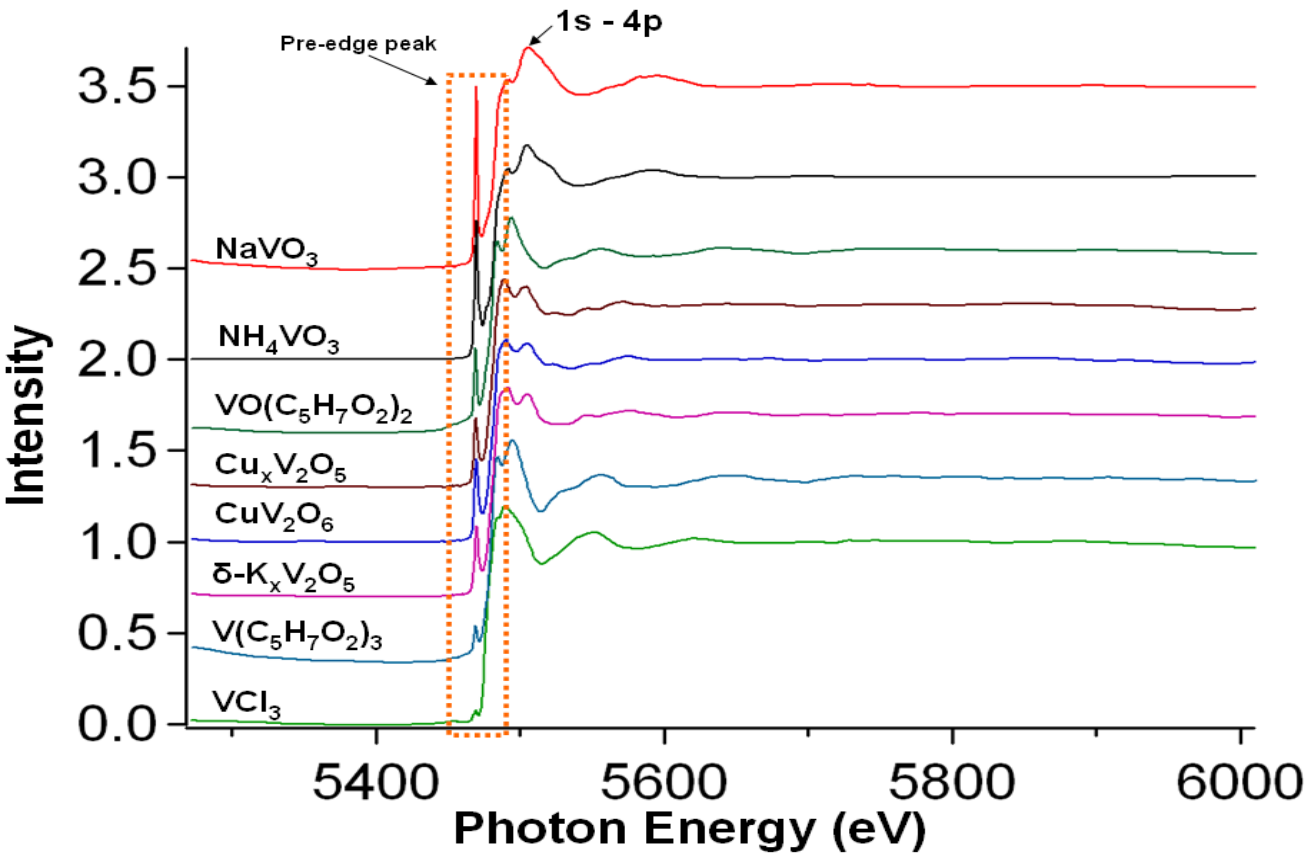

Figure S9. V K-edge XAFS spectra obtained at room temperature for several ternary vanadium phases with known coordination environments that serve as standards for Figures 6B and C.

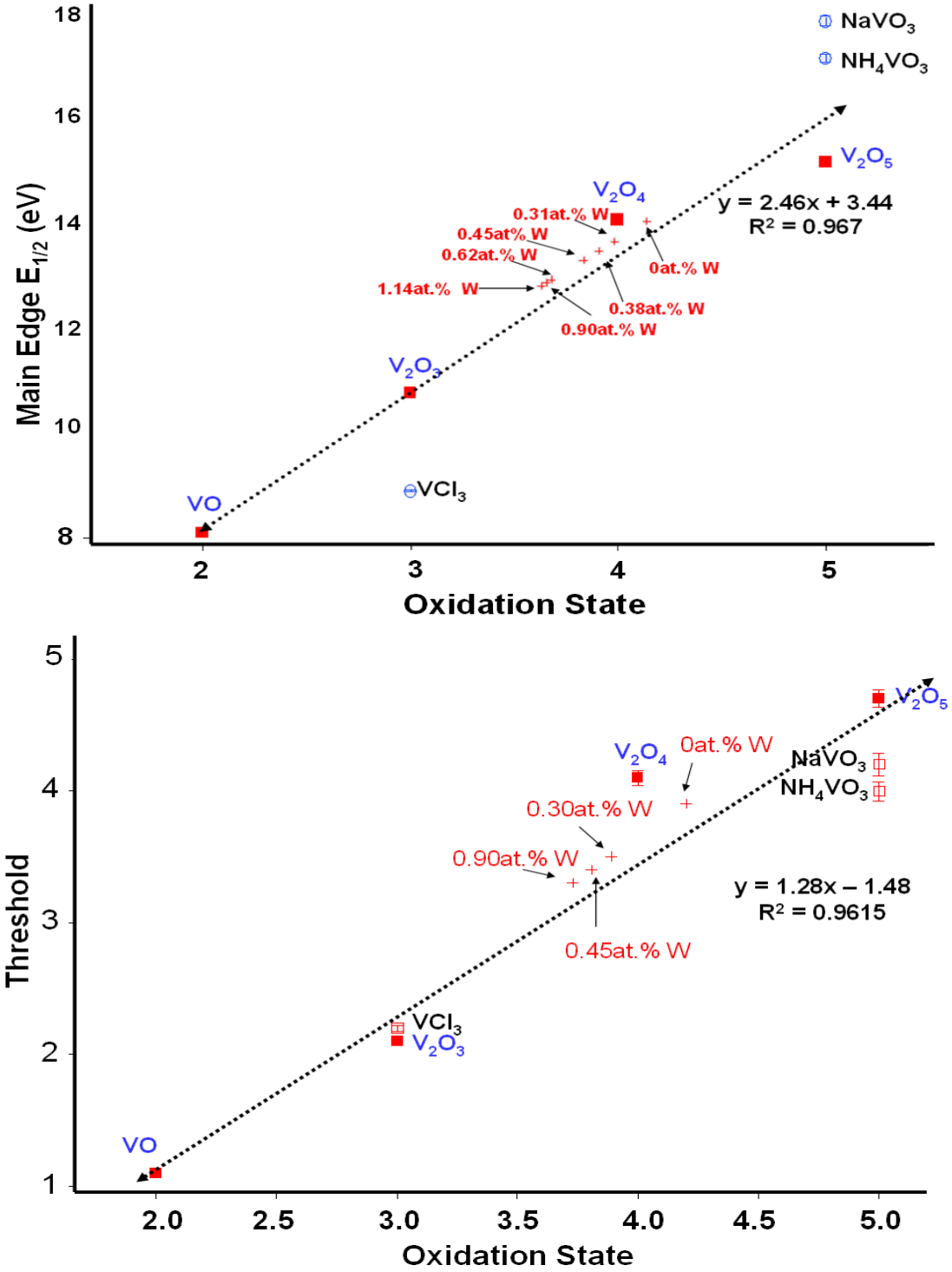

Figure S10. Plots of the main edge $E_{1/2}$ and threshold measured at the vanadium K-edge plotted as a function of the formal vanadium oxidation state with measurements for the $W_xV_{1-x}O_2$ nanobelts indicated on these calibration curves. The as-synthesized $W_\delta V_{1-\delta}O_2$ nanobelts were fitted using the method of Chaurand,[56] which provides a good method to obtain insight into the symmetry and oxidation state of V atoms.

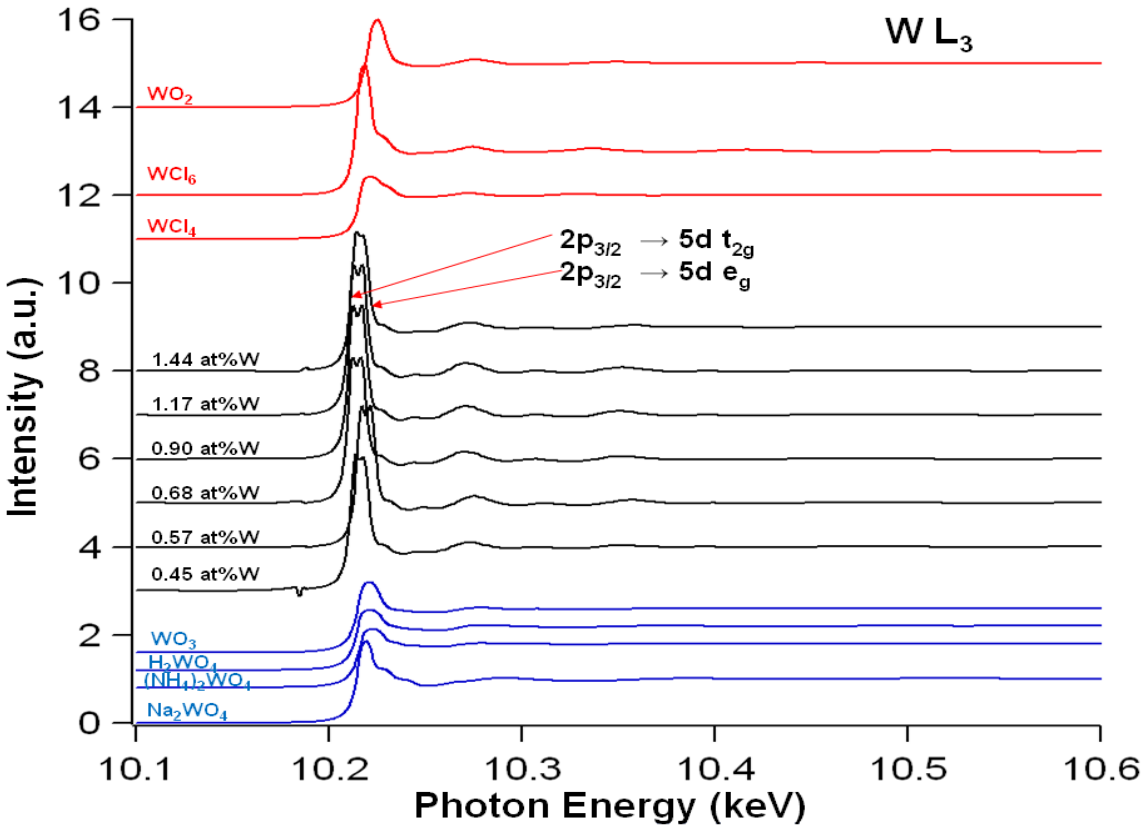

Figure S11. XANES and EXAFS W L_{III} spectra for several as-prepared $W_xV_{1-x}O_2$ nanobelts and standards.